Biologically inspired flexible photonic films for efficient passive radiative cooling

Haiwen Zhang[a], Kally C. S. Ly[a], Xianghui Liu[a], Zhihan Chen[a,b], Max Yan[c], Zilong Wu[b], Xin Wang[a], Yuebing Zheng[b], Han Zhou[a,1], and Tongxiang Fan[a,1]

[a]State Key Laboratory of Metal Matrix Composites, School of Materials Science and Engineering, Shanghai Jiao Tong University, 200240 Shanghai, China; [b]Walker Department of Mechanical Engineering, Materials Science & Engineering Program, Texas Materials Institute, The University of Texas at Austin, Austin, TX 78712; and [c]Department of Applied Physics, School of Engineering Sciences, KTH Royal Institute of Technology, 16440 Kista, Sweden

Edited by David A. Weitz, Harvard University, Cambridge, MA, and approved May 7, 2020 (received for review January 30, 2020)

Temperature is a fundamental parameter for all forms of lives. Natural evolution has resulted in organisms which have excellent thermoregulation capabilities in extreme climates. Bioinspired materials that mimic biological solution for thermoregulation have proven promising for passive radiative cooling. However, scalable production of artificial photonic radiators with complex structures, outstanding properties, high throughput, and low cost is still challenging. Herein, we design and demonstrate biologically inspired photonic materials for passive radiative cooling, after discovery of longicorn beetles' excellent thermoregulatory function with their dual-scale fluffs. The natural fluffs exhibit a finely structured triangular cross-section with two thermoregulatory effects which effectively reflects sunlight and emits thermal radiation, thereby decreasing the beetles' body temperature. Inspired by the finding, a photonic film consisting of a micropyramid-arrayed polymer matrix with random ceramic particles is fabricated with high throughput. The film reflects ∼95% of solar irradiance and exhibits an infrared emissivity >0.96. The effective cooling power is found to be ∼90.8 W·m^{-2} and a temperature decrease of up to 5.1 °C is recorded under direct sunlight. Additionally, the film exhibits hydrophobicity, superior flexibility, and strong mechanical strength, which is promising for thermal management in various electronic devices and wearable products. Our work paves the way for designing and fabrication of high-performance thermal regulation materials.

bioinspired materials | flexible photonic film | passive radiative cooling | thermoregulation

Conventional cooling devices, such as refrigerators and air conditioners, consume a fair amount of energy and resources and generate extra heat during operation, which bring about the greenhouse effect and the urban heat island effect (1). As an innovative and environmentally friendly alternative, the recently emerged passive radiative-cooling materials can be used for achieving energy-efficient buildings (2, 3), efficient solar cells (4, 5), novel cooling fabrics (6–9), and supplemental cooling systems for power plants (10, 11). The key to achieve a lower temperature than that of the surroundings even under direct sunlight is to have a high reflectivity to repel incoming sunlight (wavelength 0.3 to 2.5 μm) and a high thermal emissivity to radiate heat to outer space in the transparent atmospheric spectral window (TASW; 8 to 13 μm) (12–17). In recent years, there have been several proposals and demonstrations of photonic structures for controlling both solar reflection and thermal emission by manipulating light–matter interactions at subwavelength scales (18–24). Rephaeli et al. (18) proposed a planar photonic structure capable of realizing passive radiative sky cooling. Thereafter, numerous inspiring photonic approaches to daytime radiative cooling were experimentally demonstrated, including one-dimensional photonic crystals with alternating layers of silicon dioxide and hafnium dioxide (19), multilayer conical metamaterial pillar arrays (20), hybrid metamaterials with resonant polar dielectric microspheres (21), and hierarchically porous polymer coatings (22). However, such materials inevitably require rational structure design and impose stringent requirements on nanofabrication to realize high reflectance/absorption efficiency with frequency selectivity. A tradeoff needs to be made between high optical/thermal performance and low-cost manufacturing. High-precision nanomanufacturing techniques that can be used are focused ion beam lithography and electron beam lithography (25, 26); both techniques are costly and usually have relatively low yield. Scalable nanomanufacturing of photonic structures with complex architectures, controlled spectral reflection/absorption selectivity, and desired properties remains a challenge.

Some natural creatures have astonishing photonic structures for thermal regulation, camouflage, signaling, and so (27–29), which motivated biomimetics (30–32). One of the fascinating phenomena is structural whiteness or silver color, which can be prevalently found in insects (33–35), aquatic organisms (36, 37), and mammals (38, 39). Over the past few years, numerous biological creatures have been reported to exhibit a thermal regulation ability (40–44). For example, silvery Saharan ants were reported to exhibit thermal control behaviors via their triangular-shaped hairs, which exhibited high reflectivity in the visible to near-infrared (vis-NIR) region and high emissivity in the mid-infrared (MIR) region (40). Silkworm silk was discovered to exhibit passive cooling due to the strong reflectivity caused by Anderson localization and the high MIR emissivity of the biomolecules (41). Very recently, our group reported that the white

Significance

Some biological creatures have astonishing photonic structures to exhibit a thermal regulation ability. Taking inspiration from the brilliantly golden longicorn beetles, we demonstrate a bioinspired design of flexible hybrid photonic films for achieving efficient passive radiative cooling. Resonant polar dielectric microsphere particles were introduced into polydimethylsiloxane with photonic architectures to enhance the visible to near-infrared reflectivity and the midinfrared emissivity, enabling considerable subambient temperature drops under direct sunlight. This work paves the way toward radiative cooling technology based on photonic radiators with high performance and large-scale production, showing great potential for energy savings and efficient power generation.

Author contributions: H. Zhang, H. Zhou, and T.F. designed research; H. Zhang and Z.C. performed research; H. Zhang and X.L. contributed new reagents/analytic tools; H. Zhang, K.C.S.L., X.L., Z.C., M.Y., Z.W., X.W., Y.Z., H. Zhou, and T.F. analyzed data; H. Zhang, K.C.S.L., and H. Zhou wrote the paper; and M.Y., Z.W., and Y.Z. revised the manuscript and provided suggestions and comments on it.

The authors declare no competing interest.

This article is a PNAS Direct Submission.

[1]To whom correspondence may be addressed. Email: hanzhou_81@sjtu.edu.cn or txfan@sjtu.edu.cn.

This article contains supporting information online at https://www.pnas.org/lookup/suppl/doi:10.1073/pnas.2001802117/-/DCSupplemental.

First published June 15, 2020.

beetle *Goliathus goliatus* with an exquisite shell/hollow cylinder structure (42) and the silvery butterfly *Curetis acuta* with irregular scales (43) exhibit broadband reflectivity and radiative heat dissipation. Many of these biological photonic structures have evolved to be hierarchical ones characterized by distinct sizes and dimensionalities of structural building blocks (45, 46). The building blocks, including nanoholes, nanorods, and nanobridges, are sequentially or randomly patterned to form integrated systems (47–49). Mimicking biophotonic solutions for thermoregulation represents a promising strategy for designing bioinspired materials for passive radiative cooling with fascinating properties.

The longicorn beetle *Neocerambyx gigas* with bright golden brilliancy, belonging to the subfamily Cerambycidae, is highly adaptable to areas of hot climate all year round. Its main habitats are widely distributed in the tropical regions of southeast Asia, including Thailand and Indonesia (50). In particular, the numerous active volcanoes in Java (115°E, 8°N) and Sumatra (102°E, 0°N) continuously radiate heat into the surroundings, increasing the ambient temperature (51). On hot summer days, the environment temperatures usually rise to above 40 °C, while the ground temperatures can even exceed 70 °C (52). During the hot period, longicorn beetles usually suspend daily foraging activities and remain still to unload excess heat. To efficiently reduce their body temperature for extended periods of time in foraging activities they have developed an efficient way to reduce heat absorption from the external environment and simultaneously dissipate excess heat. The beetles' survival in such extreme conditions suggests possible thermoregulation ability of their body structures.

In this work, we discover indeed that the dual-scale triangular-shaped fluffs, characteristic of *N. gigas*, enable the tropical beetles to decrease their body temperature by increasing the reflectivity in the vis-NIR region based on total internal reflection and Mie scattering and by enhancing the MIR emissivity to radiate heat to the surroundings. Taking inspiration from the brilliantly golden longicorn beetles, we demonstrate a bioinspired design of flexible hybrid photonic films for achieving efficient passive radiative cooling. The films are fabricated by a facile microstamping method, which is promising for scale-up production. The bioinspired radiative cooling (Bio-RC) film consists of micropyramid periodic arrayed polydimethylsiloxane (PDMS) encapsulating randomly distributed spherical ceramic particles (e.g., Al_2O_3, TiO_2, and ZnO). Owing to the efficient Mie scattering of the encapsulated particles and the total internal reflection of the photonic architecture in the vis-NIR region, the Bio-RC film exhibits extremely high reflectance for solar light and simultaneously high emissivity at MIR due to the strong absorption of the resonant polar dielectric microspheres assisted further by the gradual refractive index change of the micropyramid arrays. A 500-μm-thick Bio-RC film without silver back-coating can reflect ~95% of solar irradiance and exhibit an average MIR emissivity of more than 0.96. We experimentally demonstrate high-performance daytime cooling of the Bio-RC film, including an average radiative cooling power of ~90.8 $W{\cdot}m^{-2}$ and a passive temperature drop of up to 5.1 °C under direct sunlight. The Bio-RC film also exhibits hydrophobicity, great flexibility, and superior strength, which are favorable for many applications. Furthermore, we demonstrate that the Bio-RC films can be potentially applied in electronic and motorized devices, such as wearable products, mobile phones, and motor vehicles, for effective temperature conditioning, illustrating the excellent interdisciplinary applicability of our films. The biologically inspired photonic film, together with the general fabrication method, can have a wide range of applicability in regulating heat flow in micro- and macroscopic systems.

Results

Morphology of Fluffs on the Forewings. Specimens of *N. gigas* were acquired from Indonesia for all of the optical and thermodynamic experiments. As shown in Fig. 1*A*, the forewings of the longicorn beetle exhibit a golden glare. Scanning electron microscopy (SEM) images revealed that the elytra are covered by tiny fluffs with a density of ~25,500 per square centimeter, as determined by the follicle estimation (Fig. 1*B* and *SI Appendix*, Fig. S1). After fade processing to remove the pigment attached to the forewings, the shiny color of the fluffs remained, suggesting that the forewings resembled reflective surfaces. As shown in Fig. 1*C*, the tapered fluffs grown out from the elytra are oriented in the same direction that is nearly perpendicular to the

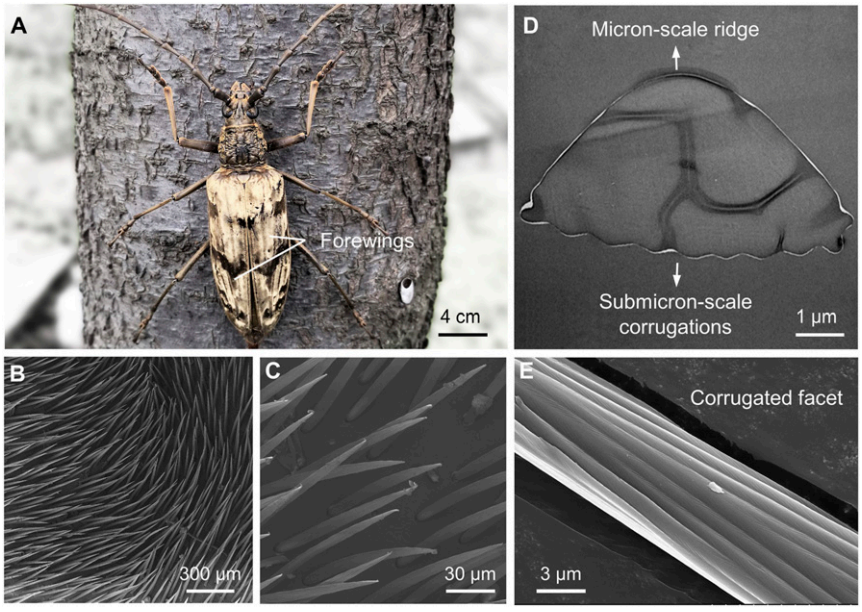

Fig. 1. Morphology characterizations of fluffs on the forewings of *N. gigas*. (*A*) Photograph of a male *N. gigas*. (*B* and *C*) SEM images of the dense fluffs covering on the forewing (*B*) and growing straight and gradually tapering off upward from the root to the tip (*C*). (*D*) Transmission electron microscopy image of the cross-sectional view of the fluff. (*E*) SEM image of the fluff with a corrugated facet.

elytra surface. The fluffs are further discovered to form upward triangular shapes from the root to the tip, leading to a dual-scale section consisting of two smooth facets and a corrugated facet with frills (Fig. 1 *D* and *E*). The corrugated facet comprises several well-arranged and distributed pleats. The size of a single pleat is ∼1 μm in width and ∼0.18 μm in height, which is an order of magnitude smaller than those of the overall triangular shape.

Optical Properties and Thermodynamic Experiments. Optical measurements of the forewings were conducted by Fourier transform spectroscopy. In the vis-NIR range, the fluffy region averagely reflected 65% of the solar irradiation, contrasted to only 30% after fluff removal (Fig. 2*A*). Moreover, the high reflectivity of the specimens disappeared after wetting them with an ethanol–water solution due to the removal of the refractive index contrast between the fluffs and air (Movie S1). When the solution evaporated, the fluffs gradually recovered, and the contrast returned, which indicated that the reflectivity variation was related to the microstructure. The recovery of the fluffs was further characterized by the time-dependent increase of reflectivity (from 10% at submerged state to 65% at evaporated state) of the fluffs during the ethanol–water solution evaporation process (Fig. 2*B*). Our results indicate that the strong broadband reflection of the forewings in the vis-NIR range is attributed to the dual-scale microstructures.

To further understand the underlying mechanism, we employed finite-difference time-domain (FDTD) simulations to investigate the optical properties of the dual-scale microstructures at different light incident angles. Cross-sectional dispersions of electromagnetic field intensity were mapped to show the flow of optical energies inside the microstructures (Fig. 2 *C* and *D*). As shown in Fig. 2*C* and *SI Appendix*, Fig. S2 *A* and *C*, incident light irradiated from the corrugated side on the triangular section at a small incident angle leads to total internal reflection. Meanwhile, the pleats with comparable length to the wavelength of incident light generate strong Mie scattering, leading to enhanced reflectivity over all incident angles (53, 54). When the facets at the smooth side are exposed to the incident light at an angle beyond 36°, total internal reflection also occurs inside the fluffs due to the triangular geometry, as shown in Fig. 2*D* and *SI Appendix*, Fig. S2 *B* and *D*. Therefore, the strong reflectivity of the forewings is attributed to the synergistic effects of the Mie scattering near the edges of the fluffs and the total internal reflection in the triangular structure, where light is captured and then reradiated out in all directions.

The optical measurements in MIR regime further show the significance of fluffs in generating high MIR emissivity in the forewings in the 8- to 13-μm TASW wavelength range. As shown in Fig. 2*E*, peak absorptivity reached to 0.94 for forewing with intact fluffs, indicating that the beetles emit their body heat to the surroundings well. Moreover, the abstracted forewing with hierarchical structures had higher emissivity over the entire TASW wavelength range compared with the bare elytra, further indicating that the dual-scale microstructures of the fluffs had the effect of enhancing MIR emissivity (*SI Appendix*, Fig. S3). According to FDTD simulations (Fig. 2*F* and *SI Appendix*, Fig. S2 *E* and *F*) of the abstracted fluffs for both incident directions, (i.e., from corrugated frill and smooth sides), the surface structures act as gradient refractive index layers (*SI Appendix*, section 2 and Fig. S4) and the average reflectivity remained low for incident angle varying from 0° to 65° across the whole TASW wavelength range. According to Kirchhoff's law of thermal radiation, a decreased reflectivity corresponds to an enhanced emissivity for an unaltered transmissivity. As a result, the broadband and wide-angle low reflectivity contribute to high MIR emissivity for enhanced radiative cooling.

Thermodynamic experiments were carried out on the forewing before and after fluff removal to verify the significance of fluffs for radiative heat dissipation. The contrastive experiments were conducted in vacuum and in still air after the forewing was put into a chamber, illuminated by a xenon lamp to simulate solar radiation (*SI Appendix*, Fig. S5). In both cases, the forewing covered by natural fluffs sustained remarkably lower steady-state temperatures than the bare forewing, with a temperature difference of ∼3.2 °C in vacuum and ∼1.5 °C in air, in accordance with the thermal camera images obtained for a more intuitive analysis in Fig. 2 *G* and *H*. The different results in the two media were attributed the combined heat-dissipating effects by thermal radiation and convection in air, while thermal convection is inhibited in vacuum. Furthermore, the time constant of the temperature change is shortened for the fluffy forewing (τ_f) compared to that for the bare forewing (τ_b), suggesting increased radiative heat transfer rate and verifying the role of fluffs in enhancing radiative heat dissipation. Theoretical calculations indicated that the fluffs enhance the emissivity by ∼11% (*SI Appendix*, section 3 and Table S1). Together with reduced solar heat gain in the vis-NIR region, it endows the longhorn beetle with a daytime radiative cooling ability. Such lower-than-environment body temperature benefits the insects in their daily foraging activities in a high-temperature environment with excessive sun exposure.

Bioinspired Photonic Design and Numerical Optimization. As revealed, the biological *N. gigas* model features a typical dual-scale microstructure composed of a triangular section with densely distributed pleats on the bottom facet (Fig. 3*A*). In this model, the pleats can result in high reflectivity in the vis-NIR region due to Mie scattering. In addition, the triangular section is responsible for the high vis-NIR reflectivity because of total internal reflection, whereas it exhibits high emissivity in the MIR range benefiting from the gradual refractive index change. Inspired by the biological model, a PDMS polymer with microstructured triangular surface undulation was used as substrate as well as matrix material. As a promising and low-cost polymer, PDMS has great prospects in passive radiative cooling owing to its transparency in the vis-NIR spectrum and strong MIR absorption/emissivity (55). The microsized pleats on the corrugated facets in the beetle model were substituted with microsized particles with similar strong Mie scattering effect. Spherical ceramic particles, such as Al_2O_3 microparticles, were embedded into the matrix for enhanced Mie scattering and facile fabrication. Al_2O_3 has negligible absorption in the vis-NIR spectral range and hence hardly generates heat under direct solar irradiance (56). At MIR, Al_2O_3 particles have strong phonon polariton resonances that can lead to further increased emissivity (*SI Appendix*, Fig. S6) (57).

FDTD simulations were conducted to investigate the optimal three-dimensional (3D) architecture. We first optimized the geometry of the microstructures. The MIR emissivity of three typical structures with triangular sections (i.e., pyramid, cone, and prism arrays) were simulated and shown in Fig. 3*B*. The refractive index applied in simulation was measured as described in *SI Appendix*, section 4 and Fig. S7. Taking the transverse electric (TE) and transverse magnetic (TM) polarizations into account, the spectra reveal that the average emissivity of the pyramid structure is higher than those of the prism or cone structures of the same feature size (*SI Appendix*, Fig. S8). Such results are attributed to the fact that the pyramid structure has an efficient gradual refractive index change for both TE and TM polarizations, while the prism structure has an efficient refractive index change only for TM polarization. The denser arrangement of pyramid units can also enhance the MIR emissivity (*SI Appendix*, Fig. S9). When the height h of a single unit is increased with the fixed bottom width w, the base angle θ ($\tan\theta = 2h/w$) changed, and the average emissivity gradually increased. As silicon template was applied for the actual fabrication process, the value of the base angle θ was restricted by the native silicon etching angle $\theta_e = 54.74°$, which is expressed as follows:

$$\theta = \arctan\left(2h/w\right) = \theta_e. \quad [1]$$

As shown by the black dotted lines ($\theta = 54.74°$) in Fig. 3*B*, when the width and the height of the pyramid structural motif are 8 μm

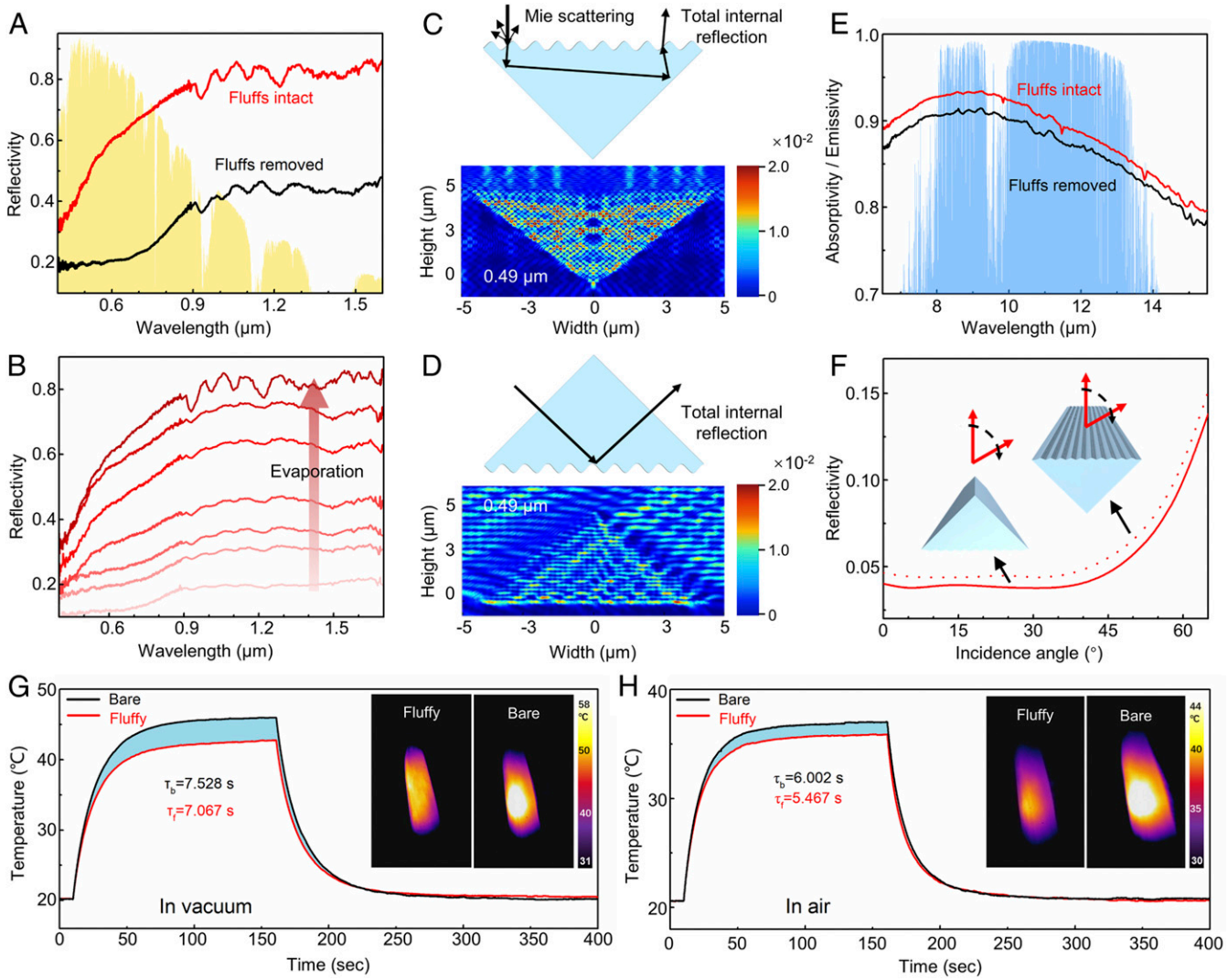

Fig. 2. Optical measurements of forewings and thermodynamic experiments. (*A*) Optical spectra of hemispherical reflectivity measured in the vis-NIR range at normal incidence, with the normalized AM 1.5 solar spectrum (yellow shaded area). (*B*) Reflectivity variation of the forewing with the color of the curves gradually deepening to represent the evaporation process of ethanol solution. (*C* and *D*) Diagrams of the visible-NIR light entering through the cross-section of the fluff model from different directions, followed by their respective electromagnetic field intensity dispersion at a wavelength of 0.49 μm. (*E*) The MIR absorptivity/emissivity of the forewings before and after fluffs removal measured at normal incidence. The light blue region represents the TASW. (*F*) Simulated average reflectivity of the abstracted fluffs with different incident angles in the 8- to 13-μm wavelength range. The feature sizes of the overall triangular section and the single pleat are 10 μm and 1 μm, respectively. (*G* and *H*) Temporal temperature profiles measured for the bare (black line) and the fluffy (red line) forewings in vacuum and in air. (*Insets*) The thermal camera images showing the forewing with and without fluffs at steady thermal states in different medium.

and 5.66 μm, respectively, the maximum average emissivity can be obtained.

We then optimized the size of the embedded spherical particles, which significantly alters the effective excitation of the Mie scattering and phonon polariton resonances. With increasing particle size, especially when the diameter was greater than 1.0 μm, the scattering efficiency of the entire solar spectrum was significantly improved (Fig. 3*C*). The simulation results were also experimentally verified by diffuse transmission measurements (*SI Appendix*, section 5 and Fig. S10). The results show that the embedded Al_2O_3 spherical particles have largely different optical responses in comparison with those of PDMS at MIR regime, which are attributed to the strong phonon polariton resonances of the microparticles. It is known that there exists a strong phonon resonance expected near 770 cm^{-1} (corresponding to 13 μm in wavelength) for Al_2O_3 particles (58). We therefore calculated the normalized absorption, scattering, and extinction cross-section efficiencies of the microspheres embedded in PDMS as a function of the size parameter for incident light at a 13-μm wavelength, as shown in Fig. 3*D*. The extinction peak occurred at a size parameter of ∼0.4, corresponding to a microsphere diameter of ∼1.7 μm. High-order Fröhlich resonances, including magnetic and electric modes, are intensely excited at the extinction peak (59). Furthermore, the MIR (wavelengths from 8 to 13 μm) emissivity of the PDMS film with embedded Al_2O_3 particles is highly dependent on the mass fraction of the microparticles in the film with fixed particle size. As shown in Fig. 3*E*, for Al_2O_3 microspheres with diameter of 2 μm, the highest value of average MIR absorptivity/emissivity can be obtained at the mass fraction of ∼50%, corresponding to an interparticle distance of 2.75 μm. The effects of the interparticle spacing can be further observed in the mapping of the electromagnetic

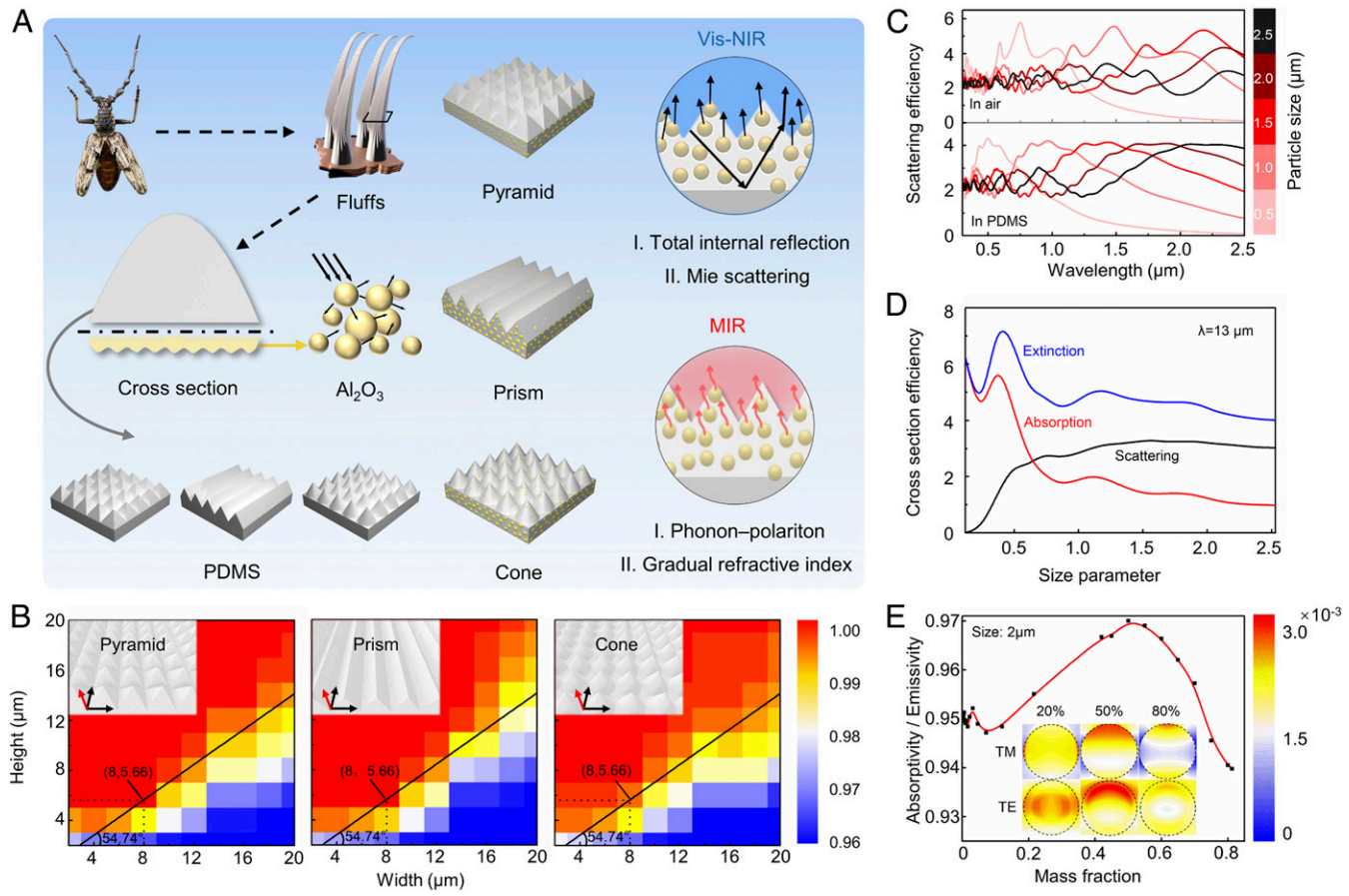

Fig. 3. Proposed bioinspired model and simulation optimizations. (*A*) Schematic diagram of the bioinspired concept from fluffs into hybrid films with photonic architectures. (*B*) Simulated average emissivity in the TASW as a function of varied width and height of the triangular section for different 3D architectures. (*C*) Simulated scattering efficiency spectra of Al_2O_3 microspheres with different sizes in air and in PDMS, respectively. (*D*) Cross-section spectra of individual Al_2O_3 microspheres as a function of size parameter illuminated at a 13-μm wavelength. (*E*) Simulated average emissivity in the range of 8 to 13 μm varying with the mass fraction of doped Al_2O_3 spherical particles. (*Insets*) TM and TE electromagnetic field intensities on cross-sectional view of 2-μm-diameter Al_2O_3 microspheres at a wavelength of 10.56 μm.

field intensity at the wavelength of 10.65 μm (Fig. 3 *E*, *Insets*). When the mass fraction is 50%, the hot spots of the TM and TE modes spatially overlap, indicating the formation of high-order Fröhlich resonances, which are similar to those at the extinction peak. As a result, the enhanced MIR emissivity to compensate for the absorption dips of PDMS (60) is attributed to the synergetic effect of strong resonance of Al_2O_3 microspheres, high-order Fröhlich resonance, and the gradual effective refractive index variation of the structured film.

Preparation and Characterization of the Bioinspired Photonic Film. According to the numerical analysis above, the optimized Bio-RC film has an array of a pyramid PDMS structure with width 8 μm and height 5.7 μm containing randomly distributed Al_2O_3 spheres with diameter around 2 μm (*SI Appendix*, Fig. S11). PDMS matrix and Al_2O_3 spheres had mass ratio of 1:1. We have measured and simulated the transmissivity and reflectivity spectra of Al_2O_3–PDMS hybrid films with different thicknesses (*SI Appendix*, section 6 and Figs. S10*D* and S12). The optimized Bio-RC films were fabricated in larger scale via the microstamping method (Fig. 4*A*). The fabrication process consisted of multiple steps including photolithography, dry etching, wet etching, spin coating, and stripping. First, photolithography and reactive ion etching were applied to pattern square arrays onto a thin silicon nitride layer on top of a (100) silicon wafer. The patterned silicon nitride layer then served as a mask to carry out anisotropic etching with potassium hydroxide (KOH), leading to inverted micropyramids on the silicon wafer (Fig. 4*B* and *SI Appendix*, Fig. S13*A*). After the anisotropic etching, the inverted pyramid silicon wafer was used as a template for rapid replication of Bio-RC films. Specifically, the Bio-RC film was conveniently fabricated in a single step by spin-coating precursor solution (i.e., PDMS with randomly distributed Al_2O_3 microsphere particles) onto the template. The coated template was thermally cured in vacuum to accelerate the solidification process. Fig. 4*C* and *SI Appendix*, Fig. S13*B* show the surface of the resulting Bio-RC film with pyramid patterns. It is worth mentioning that the sizes of features on the Bio-RC film were identical to those of the microstructures on the silicon template. Furthermore, a subsequent facile secondary spin coating (Fig. 4*A*) was applied to obtain a large-scale Bio-RC film in a 30-cm-wide roll (Fig. 4*D*). The scalability of our fabrication procedure makes it promising for practical applications requiring large-area films.

The Bio-RC film has a rather whitish appearance (i.e., strong broadband reflectance in visible spectrum). As shown in Fig. 4 *E* and *F*, the microspheres are randomly distributed in the fabricated film, with micropyramid arrays well-arranged on the surface. It is worth mentioning that the microstamping method developed here is generic, which can be generalized for obtaining a series of PDMS-based photonic hybrid films with various embedded ceramic particles, including ZnO, ZrO_2, Y_2O_3, TiO_2, MgO, and so on. Inclusion of different particles enables Bio-RC

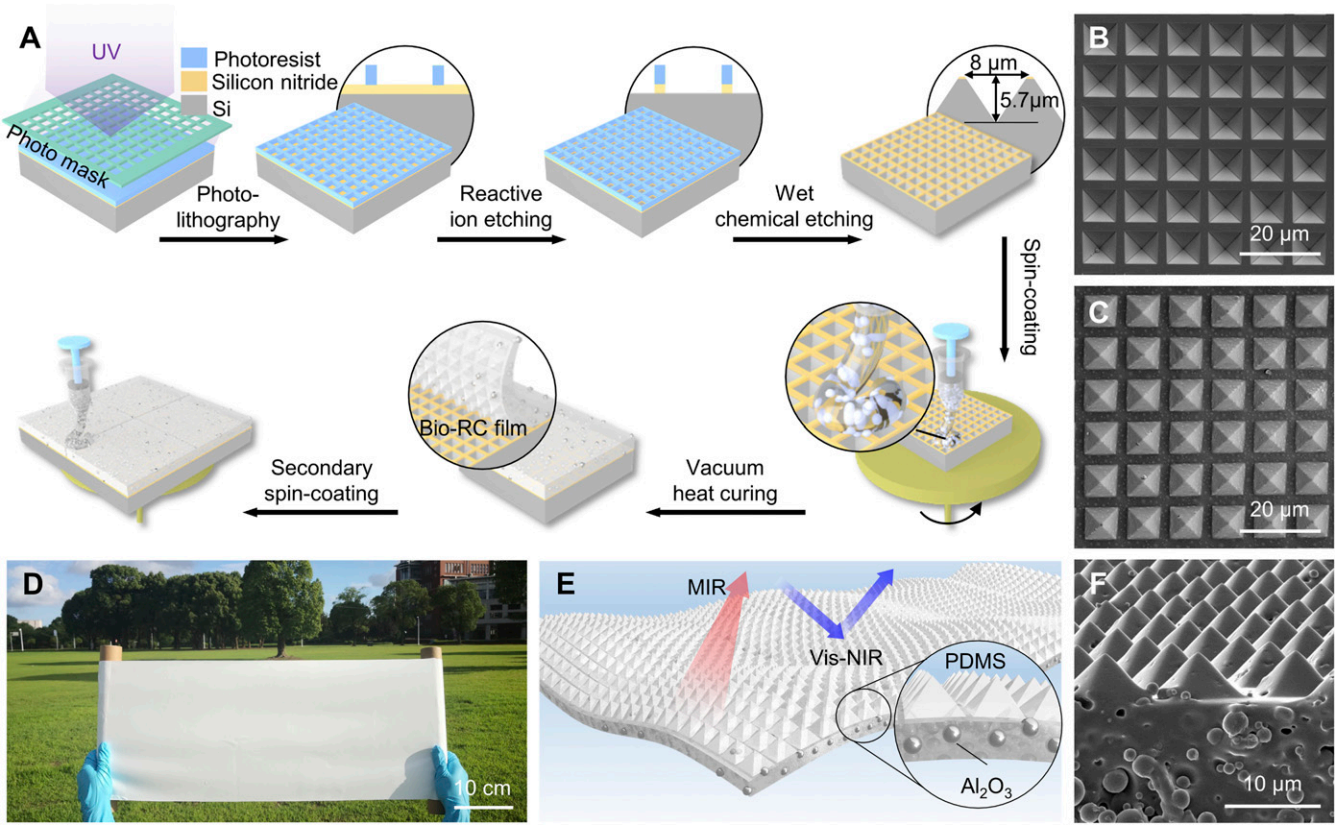

Fig. 4. Preparation and morphology of the Bio-RC film. (*A*) Schematic illustration of the preparation process of the template and the hybrid film with photonic architectures. (*B* and *C*) SEM image of the fabricated inverted-micropyramid silicon template (*B*) and the top view of the Bio-RC film (*C*) via a facile microstamping method. (*D*) Photo of the fabricated Bio-RC film on a 30-cm-wide roll. (*E*) Schematic illustration of the bioinspired flexible hybrid films. Ceramic particles are embedded in the PDMS matrix filled by compact arrays of micropyramids. (*F*) SEM image of the section of the Bio-RC film.

films with tailored optical spectral responses for a wide variety of applications. Visually, all these films exhibit a glossy white appearance (*SI Appendix*, Fig. S14). Our results indicate that the fabrication technique provides diverse possibilities for manufacturing both generic and specialized Bio-RC films.

Optical Properties and Daytime Radiative Cooling Performance of the Bio-RC Film. The fabricated Bio-RC film was quantitatively characterized by its spectroscopic performance in the solar and IR regions (Fig. 5*A*). For a 500-μm-thick Bio-RC film measured at a normal incident angle, the average reflectivity in the solar spectral range was ∼95% even without metal coating, and the average emissivity in the TASW was >0.96, which are higher than those of the flat PDMS film with randomly embedded Al_2O_3 nanoparticles. The average vis-NIR reflectivity of the contrast flat film is only 29%, which is attributed to the fact that the elimination of the pyramid photonic architectures and the smaller diameter of the Al_2O_3 particles suppress the effects of total internal reflection and Mie scattering, respectively. Meanwhile, the emissivity of the contrast flat film in the TASW is also much lower than that of the Bio-RC film due to the absence of efficient gradual refractive index. In addition, the effects of the pure pyramid photonic arrays embedded with 2-μm Al_2O_3 particles on the optical properties were examined (*SI Appendix*, Fig. S15), which verified the total internal reflection and the gradual refractive index changed induced by the micropyramid arrays. In particular, FDTD simulations of the Bio-RC film further show remarkably high MIR emissivity that persists to large angles (Fig. 5*B*). Specifically, the average MIR emissivity is higher than 90% for latitudes from 0° to 70° at all longitudes, revealing excellent radiative cooling capability of the Bio-RC film in a very wide angular range.

The actual radiative cooling capability of a Bio-RC film was characterized in Shanghai (121°25′12″E, 31°1′12″N, 4-m altitude) in late May employing the home-built setup shown in Fig. 5*C*. To achieve better accuracy, it is crucial to minimize the influence of thermal convection and conduction in the experiment, which could overwhelm the cooling power of the film. For instance, the setup consisted a polyethylene film as sealing layer above the Bio-RC film for avoiding convection as well as providing high transparency over an ultrabroadband wavelength range. In addition, a polyurethane board was used to support the Bio-RC film to reduce thermal conduction. The Bio-RC film placed in the setup was subjected to direct sunlight under a clear sky. Temperatures of both the environment (air) and the film were registered during the hottest period of the day (Fig. 5*D*). The corresponding subambient temperature drop (ΔT) can be obtained by subtracting the two temperature curves, as shown in Fig. 5*E*. Promisingly, under an average solar intensity I_{solar} of ∼862 $W{\cdot}m^{-2}$ and a humidity of 22.7% at noon (Fig. 5 *F* and *G*), the Bio-RC film achieved a high average ΔT of 5.1 °C and a high maximum ΔT of 7 °C. We further experimentally measured the cooling power by a thermal device that quantifies the thermal power needed to compensate for the temperature drop. The average daytime radiative cooling power of the film was obtained as 90.8 $W{\cdot}m^{-2}$ for the experimental conditions (Fig. 5*H*). In theory, the cooling power of the Bio-RC film calculated by theoretical equations (*SI Appendix*, section 7 and Fig. S16) is 99.8 $W{\cdot}m^{2}$, considering a 32 °C (305 K) ambient temperature without any thermal convection or conduction. The experimental result is expected to be slightly lower than the calculated ones since thermal convection and conduction were

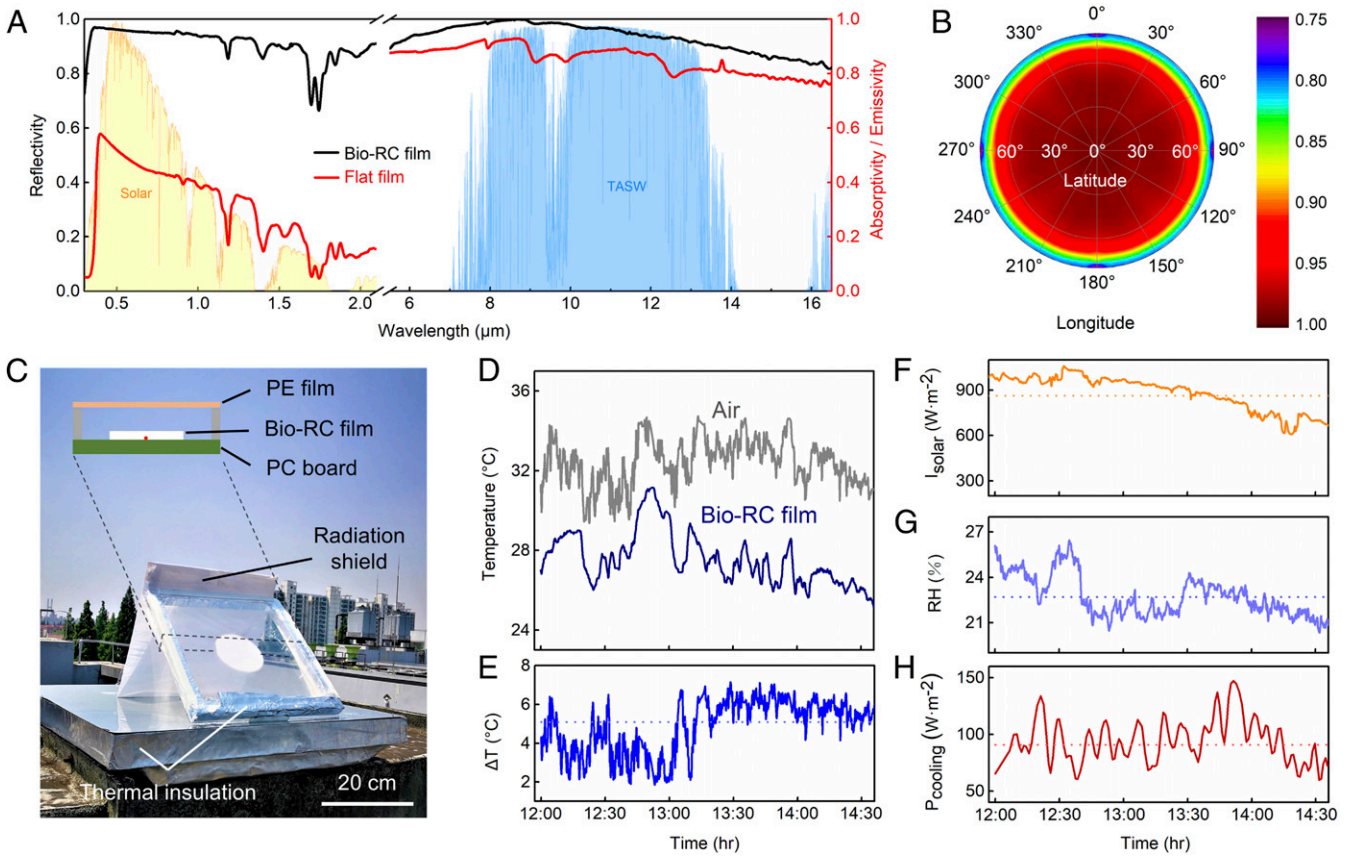

Fig. 5. Optical properties and daytime radiative cooling performance of the Bio-RC film. (*A*) Comparative experimental reflectivity (black line) in normalized ASTM G173 global solar spectrum and absorptivity/emissivity in the TASW (red line) between a 500-μm-thick Bio-RC film and a flat PDMS film with randomly embedded 100-nm-diameter Al_2O_3 particles. (*B*) Simulated average absorptivity/emissivity in the TASW for varied latitude and longitude of the incident light. (*C*) Image of the setup for daytime radiative cooling performance measurements. (*D*) Temporal temperature data of the air and the Bio-RC film under direct sunlight and (*E*) the subambient temperature drop (ΔT) of the Bio-RC film. The dotted line in *E* indicates average ΔT, which is 5.1 °C. (*F*–*H*) Detailed average solar intensity I_{solar} (*F*), relative humidity (*G*), and radiative cooling power $P_{cooling}$ (*H*) measured in the experiment in *D* and *E*; the average values of each curve in *F*–*H* are 862 W·m^{-2}, 22.7%, and 90.8 W·m^{-2}, respectively, shown as a dotted line in the corresponding graph.

minimized but not completely eliminated. Thus, we have shown that the experimental results coincide quite well with the theoretical calculations. In comparison with state-of-the-art radiative cooling materials, the fabricated Bio-RC films have shown remarkable performance, as detailed in *SI Appendix*, Table S2. Moreover, we performed a parallel experiment in the same location for all daytime hours employing an adapted setup, in which the Bio-RC film was carried inside a Dewar bottle instead of supported by the polycarbonate (PC) platform (*SI Appendix*, Fig. S17). The results demonstrated that the Bio-RC film cannot only cool itself down but can also successfully reduce the temperature of the surrounding environment and devices or hot bodies coated by the film.

Other Potential Applications. In addition to excellent optical performance, the Bio-RC film demonstrates superior behaviors in terms of hydrophobic and mechanical properties. First, the bioinspired surfaces consisting of the microscale architectures constitute a hierarchical structure, leading to a higher hydrophobicity of the film. By dripping dyed water onto the Bio-RC film, we observed the formation of spherical droplets. The closely positioned drops drew clear patterns without spreading over the Bio-RC film (Fig. 6*A*). The higher hydrophobicity due to the microtextured hydrophobic surface can be proved by contact angle (CA) measurement results. A flat film with the same material composition without a microtextured surface is applied for comparison. As shown in Fig. 6*B*, the Bio-RC film has a high CA of ∼138°, which is more than 20% higher than that of the flat film (∼114°). The higher hydrophobicity of the Bio-RC film could foreseeably have important impacts on the development of many potential practical applications, including self-cleaning, antifouling, and corrosion prevention (Movie S2). In addition, our Bio-RC film sustained its excellent mechanical properties after repeated mechanical deformation, such as alternative twist and stretch for hundreds of times (Fig. 6*C*). The excellent flexibility and elasticity suggest that the Bio-RC films can endure mechanical shocks and dynamic deformations, which is crucial for longer durability and broader applications.

Practically, radiative cooling devices can be widely applied in various energy-saving thermal management systems, such as cooling systems for buildings, personal devices, and even our bodies. Utilizing the stain resistance, mechanical fracture resistance, and passive radiative cooling capacity of the Bio-RC films, we have demonstrated various potential applications in daily activities. For instance, the hydrophobic film can be used as an umbrella coating that repels waterborne dirt (Fig. 6*D*). The excellent ultraviolet light reflectance and exceptional daytime radiative cooling ability can further extend the functional quality of the umbrella. In addition, the excellent flexibility and thermal comfort make the Bio-RC films good candidates in wearable products to cool down human bodies during hot days, as shown by the thermal image in Fig. 6*E*. We envision that the Bio-RC

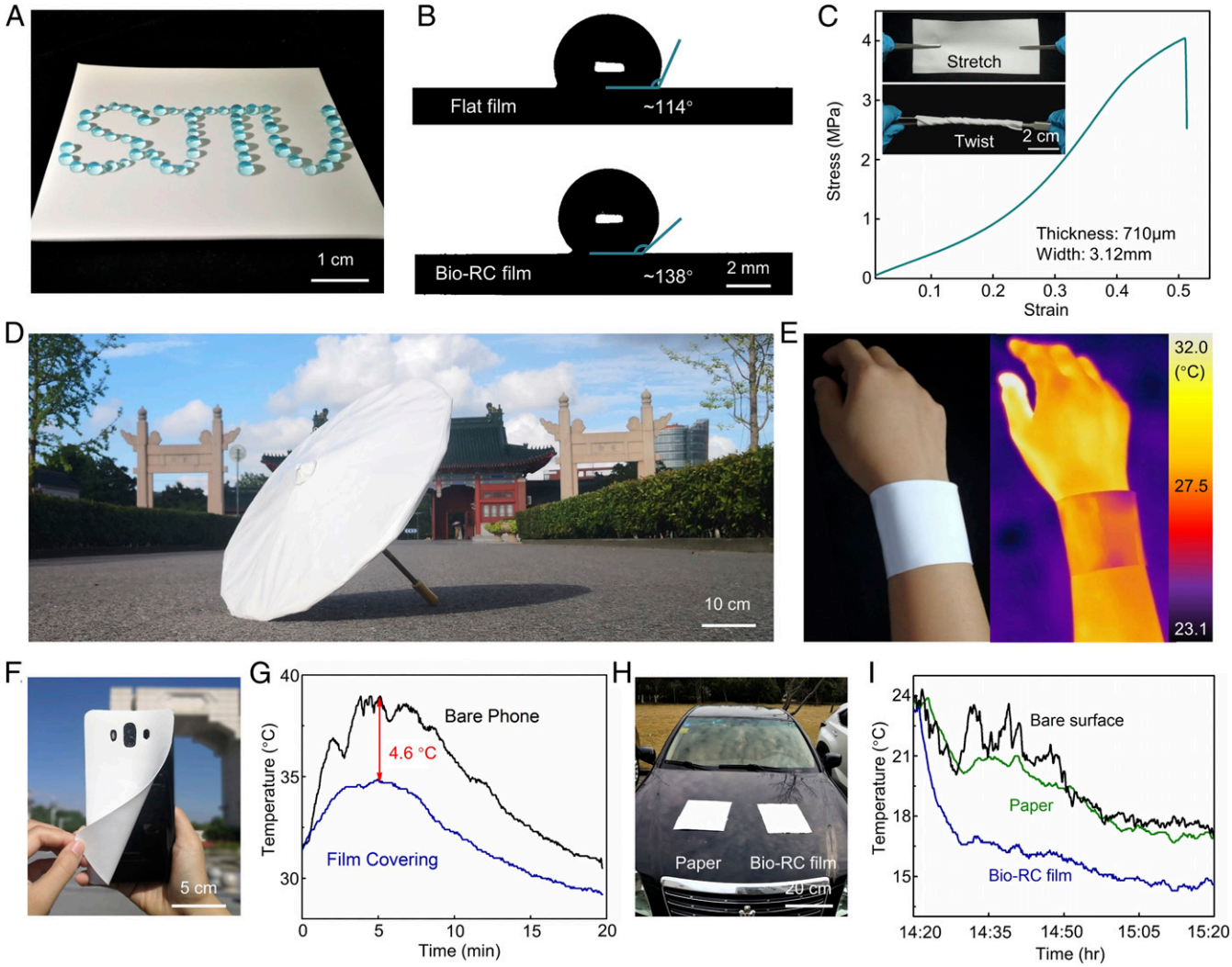

Fig. 6. Additional properties and potential applications of the Bio-RC film. (*A*) Photograph of a hydrophobic Bio-RC film sustaining dyed spherical water drops. (*B*) Comparison of CAs between a flat film and the Bio-RC film with the same components. (*C*) Stress–strain curve of the Bio-RC film. *Insets* show that the film remained intact and remarkable mechanical damage was not observed through hundreds of twists and stretches. (*D*) Photograph of an umbrella made of Al_2O_3–PDMS hybrid films, suitable for both sunny and rainy days. (*E*) Demonstration of the potential application of the film in wearable devices. (*F*) Mobile phone covered with the film tailored for its shape and size for cooling purposes. (*G*) Temperature tracking for a bare phone and the phone covered with the film, running the same application under the same environmental conditions. (*H* and *I*) Digital picture and corresponding temperature variation of a piece of paper and the Bio-RC film with the similar size and thickness on the surface of a car hood.

films could be further integrated into skin-contacting wearable electronics to reduce the uncomfortable heating effects of electronic devices. In another example, a Bio-RC film was cut and fitted onto a mobile phone. After running a specific application on the mobile phone for 20 min under a clear sky, its temperature was recorded and compared to the case without the Bio-RC film. A maximum temperature drop of 4.6 °C was observed for the coated device (Fig. 6 *F* and *G*). Moreover, the outstanding cooling performance of our Bio-RC film applied to vehicles was verified as shown in Fig. 6 *H* and *I*. We performed a 60-min experiment and simultaneously tracked the temperatures of the Bio-RC film and white paper with a similar size and thickness which were placed on the surface of a car hood and exposed to the sunlight. The Bio-RC film achieved a higher average ΔT of 3.8 °C and a higher maximum ΔT over 7 °C, whereas the white paper could cool the car by an average ΔT of only 0.6 °C. The significant differences are attributed to the vis-NIR optical reflectivity and MIR thermal emissivity (*SI Appendix*, Fig. S18). Such strong cooling effects show that the Bio-RC films are promising passive cooling materials for electronic devices (i.e., mobile phones, laptops, and touchpads) and motor vehicles.

Discussion

To summarize, we have proposed and demonstrated a generic method to fabricate bioinspired flexible hybrid films with photonic architectures for efficient passive radiative cooling. The tropical longicorn beetle *N. gigas* was identified to have a dense array of bright shiny fluffs with a triangular cross-section with one side decorated with pleats. These dual-scale microstructures effectively increased reflectivity over the solar spectral regime and enhanced emissivity in the MIR spectral regime. The combined effects lead to decreasing of the beetle's body temperature for coping with high environmental temperatures. Inspired by the biological model, we then proposed with the help of numerical simulation a flexible photonic hybrid film with micropyramid surface structuring and embedded dielectric microparticles. Sample films based on PDMS and ceramic microparticles were fabricated via a high-throughput and large-scale microstamping fabrication method.

Their optical and radiative-cooling performances were experimentally verified. Resonant polar dielectric microsphere particles were introduced into PDMS with photonic architectures to enhance the vis-NIR reflectivity and the MIR emissivity, enabling considerable subambient temperature drops under direct sunlight. Furthermore, the flexibility and hydrophobicity of the fabricated Bio-RC films can have added values for incorporating such films in various radiative cooling systems, including wearable and personal electronic devices and motor vehicles. Our work paves the way toward radiative cooling technology based on photonic radiators with high performance and large-scale production, showing great potential in energy savings and efficient power generation.

Materials and Methods

Pigment and Fluffs Removal of Forewings. The longicorn beetle specimens were bought from Shanghai Qiuyu Biotechnology Co., Ltd. The forewings of the longicorn beetles were cut off using a sharp blade for investigation. The obtained forewings were rinsed with ethyl alcohol and water alternately to remove impurities attached to the surfaces. For pigment removal, the forewings were completely immersed in a 10% hydrogen peroxide (H_2O_2) solution for 48 h and then rinsed thoroughly with purified water. For fluffs removal, we used a blunt tungsten needle to gently rub the surfaces. The broken fluffs were easily attached to the needle due to electrostatic interactions.

Bio-RC Films Preparation. The silicon template was prepared by multiple combinatorial etching. In the first step, the photoresist was evenly applied to the silicon wafer with (100) crystal plane orientation, coated with 100-nm-thick silicon nitride (Si_3N_4) to transfer the topography of the lithographic mask to the photoresist. The mask was designed to be arrays of square pores with a size of 8 μm × 8 μm. The width of the joint was 2 μm. After the lithography operation, reactive ion etching was performed on the silicon wafer to remove the exposed silicon nitride and release the silicon substrate. The silicon wafer was then wet-etched for anisotropic treatment. The formula of silicon corrosion liquid was a mixture of KOH, isopropyl alcohol, and H_2O in a ratio of 1:2:2. The etching angle was 54.74°. When the etching solution reached the bottom tip of the silicon, the chemical reaction stopped. After that, the etched silicon wafer was cleaned to remove residual photoresist and silicon nitride from the surface. Finally, the template was deposited a layer of fluorocarbon film to make the Bio-RC films easy to peel off from the silicon chip. The Bio-RC films were fabricated by dual-spin coating stripping technique. First, the ceramic/PDMS precursor solution was prepared. Typically, Al_2O_3 spherical powder with a particle size of ∼2 μm measured by laser particle analyzer (S3500; Microtrac) was purchased from NOVORAY. The spherical powder was first dissolved in PDMS (SYLGARD 184), which was purchased from Dow Corning, and then the curing agent SYLGARD 184 silicon elastomer was added in, forming the Al_2O_3–PDMS–curing-agent precursor solution in an 11:10:1 mass ratio. In addition, the precursor solution was vacuumed for over 30 min at room temperature. Afterward, the bioinspired template was placed on the homogenizer. The Al_2O_3–PDMS precursor solution was poured on the bioinspired template. By increasing the speed and time of the homogenizer, films with different thicknesses were obtained. Next, the template coated with the solution was transferred to a heating platform for curing. The platform was heated up to 80 °C and the duration of heat treatment was 2 h. Then, it slowly cooled down to ambient temperature and the precursor solution was solidified. Finally, the Bio-RC film was obtained by peeling the film off the silicon wafer. After being executed multiple times, the obtained Bio-RC films were cut into square pieces and lined up neatly on a PC board. The side of the film with the photonic architecture was faced toward the board to prevent the structures from being destroyed and covered up. The operations of spin coating and curing were conducted above the films to piece them together. The precursor solution in the spin coatings retained the same original ingredients to blend the films well. The flat films with the embedded 100-nm-diameter Al_2O_3 particles were fabricated by the above-mentioned method. The Al_2O_3-PDMS precursor solution was poured and spin-coated on a smooth PC plate. Other ceramic powder particles with similar sizes such as zirconium oxide (ZrO_2), zinc oxide (ZnO), titanium oxide (TiO_2), and magnesium oxide (MgO) were mixed with PDMS respectively to prepare a series of PDMS/ceramic bioinspired hybrid films following the same procedures.

Characterization and other experiments can be found in *SI Appendix*.

Data Availability. All data needed to evaluate the conclusions of the paper are present in the main text, *SI Appendix*, or Movies S1 and S2.

ACKNOWLEDGMENTS. This work was supported by the Foundation for National Natural Science Foundation of China Grants 51425203 and 51772191, Natural Science Foundation of Shanghai Grant 17ZR1441100, Key Project of Intergovernmental International Scientific and Technological Innovation Cooperation Grant 2017YFE0127100, and the Top Young Talents of Ten Thousand Talents Plan. We thank the Center for Advanced Electronic Materials and Devices for technical support.

1. J. N. Munday, Tackling climate change through radiative cooling. *Joule* **3**, 2057–2060 (2019).
2. E. A. Goldstein, A. P. Raman, S. Fan, Sub-ambient non-evaporative fluid cooling with the sky. *Nat. Energy* **2**, 17143 (2017).
3. T. Li *et al.*, A radiative cooling structural material. *Science* **364**, 760–763 (2019).
4. W. Li, Y. Shi, K. Chen, L. Zhu, S. Fan, A comprehensive photonic approach for solar cell cooling. *ACS Photonics* **4**, 774–782 (2017).
5. L. Zhu, A. P. Raman, S. Fan, Radiative cooling of solar absorbers using a visibly transparent photonic crystal thermal blackbody. *Proc. Natl. Acad. Sci. U.S.A.* **112**, 12282–12287 (2015).
6. X. A. Zhang *et al.*, Dynamic gating of infrared radiation in a textile. *Science* **363**, 619–623 (2019).
7. Y. Peng *et al.*, Nanoporous polyethylene microfibres for large-scale radiative cooling fabric. *Nat. Sustain.* **1**, 105–112 (2018).
8. P.-C. Hsu *et al.*, Radiative human body cooling by nanoporous polyethylene textile. *Science* **353**, 1019–1023 (2016).
9. L. Cai *et al.*, Temperature regulation in colored infrared-transparent polyethylene textiles. *Joule* **3**, 1478–1486 (2019).
10. A. K. Stark, J. F. Klausner, An R&D strategy to decouple energy from water. *Joule* **1**, 416–420 (2017).
11. D. Zhao *et al.*, Subambient cooling of water: Toward real-world applications of daytime radiative cooling. *Joule* **3**, 111–123 (2019).
12. S. Catalanotti *et al.*, The radiative cooling of selective surfaces. *Sol. Energy* **17**, 83–89 (1975).
13. C. G. Granqvist, A. Hjortsberg, T. S. Eriksson, Radiative cooling to low temperatures with selectivity IR-emitting surfaces. *Thin Solid Films* **90**, 187–190 (1982).
14. T. M. J. Nilsson, G. A. Niklasson, Radiative cooling during the day: Simulations and experiments on pigmented polyethylene cover foils. *Sol. Energy Mater. Sol. Cells* **37**, 93–118 (1995).
15. L. Zhou *et al.*, A polydimethylsiloxane-coated metal structure for all-day radiative cooling. *Nat. Sustain.* **2**, 718–724 (2019).
16. X. Wang *et al.*, Scalable flexible hybrid membranes with photonic structures for daytime radiative cooling. *Adv. Funct. Mater.* **30**, 1907562 (2020).
17. A. Shahsafi *et al.*, Temperature-independent thermal radiation. *Proc. Natl. Acad. Sci. U.S.A.* **116**, 26402–26406 (2019).
18. E. Rephaeli, A. Raman, S. Fan, Ultrabroadband photonic structures to achieve high-performance daytime radiative cooling. *Nano Lett.* **13**, 1457–1461 (2013).
19. A. P. Raman, M. A. Anoma, L. Zhu, E. Rephaeli, S. Fan, Passive radiative cooling below ambient air temperature under direct sunlight. *Nature* **515**, 540–544 (2014).
20. M. M. Hossain, B. Jia, M. Gu, A metamaterial emitter for highly efficient radiative cooling. *Adv. Opt. Mater.* **3**, 1047–1051 (2015).
21. Y. Zhai *et al.*, Scalable-manufactured randomized glass-polymer hybrid metamaterial for daytime radiative cooling. *Science* **355**, 1062–1066 (2017).
22. J. Mandal *et al.*, Hierarchically porous polymer coatings for highly efficient passive daytime radiative cooling. *Science* **362**, 315–319 (2018).
23. S. Y. Jeong, C. Y. Tso, Y. M. Wong, C. Y. H. Chao, B. Huang, Daytime passive radiative cooling by ultra emissive bio-inspired polymeric surface. *Sol. Energy Mater. Sol. Cells* **206**, 110296 (2020).
24. D. G. Baranov *et al.*, Nanophotonic engineering of far-field thermal emitters. *Nat. Mater.* **18**, 920–930 (2019).
25. J. Ziegler *et al.*, Deterministic quantum emitter formation in hexagonal boron nitride via controlled edge creation. *Nano Lett.* **19**, 2121–2127 (2019).
26. R. Zandi Shafagh, A. Vastesson, W. Guo, W. van der Wijngaart, T. Haraldsson, E-Beam nanostructuring and direct click biofunctionalization of thiol-ene resist. *ACS Nano* **12**, 9940–9946 (2018).
27. H. Zhou *et al.*, Bio-inspired photonic materials: Prototypes and structural effect designs for applications in solar energy manipulation. *Adv. Funct. Mater.* **28**, 1705309 (2018).
28. R. Pérez-de la Fuente *et al.*, Early evolution and ecology of camouflage in insects. *Proc. Natl. Acad. Sci. U.S.A.* **109**, 21414–21419 (2012).
29. A. Krishna *et al.*, Infrared optical and thermal properties of microstructures in butterfly wings. *Proc. Natl. Acad. Sci. U.S.A.* **117**, 1566–1572 (2020).
30. S. Yi *et al.*, Subwavelength angle-sensing photodetectors inspired by directional hearing in small animals. *Nat. Nanotechnol.* **13**, 1143–1147 (2018).
31. Y. Hou, M. Yu, X. Chen, Z. Wang, S. Yao, Recurrent filmwise and dropwise condensation on a beetle mimetic surface. *ACS Nano* **9**, 71–81 (2015).
32. M. Zhu *et al.*, Tree-inspired design for high-efficiency water extraction. *Adv. Mater.* **29**, 1704107 (2017).
33. P. Vukusic, B. Hallam, J. Noyes, Brilliant whiteness in ultrathin beetle scales. *Science* **315**, 348 (2007).

34. A. Levy-Lior *et al*., Guanine-based biogenic photonic-crystal arrays in fish and spiders. *Adv. Funct. Mater.* **20**, 320–329 (2010).
35. S. Kariko *et al*., Structural origins of coloration in the spider *Phoroncidia rubroargentea* Berland, 1913 (Araneae: Theridiidae) from Madagascar. *J. R. Soc. Interface* **15**, 20170930 (2018).
36. D. Gur, B. Leshem, D. Oron, S. Weiner, L. Addadi, The structural basis for enhanced silver reflectance in Koi fish scale and skin. *J. Am. Chem. Soc.* **136**, 17236–17242 (2014).
37. G. R. Bell *et al*., Diffuse white structural coloration from multilayer reflectors in a squid. *Adv. Mater.* **26**, 4352–4356 (2014).
38. Y. Cui, H. Gong, Y. Wang, D. Li, H. Bai, A thermally insulating textile inspired by polar bear hair. *Adv. Mater.* **30**, e1706807 (2018).
39. A. Du *et al*., Multifunctional silica nanotube aerogels inspired by polar bear hair for light management and thermal insulation. *Chem. Mater.* **30**, 6849–6857 (2018).
40. N. N. Shi *et al*., Thermal physiology. Keeping cool: Enhanced optical reflection and radiative heat dissipation in Saharan silver ants. *Science* **349**, 298–301 (2015).
41. S. H. Choi *et al*., Anderson light localization in biological nanostructures of native silk. *Nat. Commun.* **9**, 452 (2018).
42. D. Xie *et al*., Broadband omnidirectional light reflection and radiative heat dissipation in white beetles Goliathus goliatus. *Soft Matter* **15**, 4294–4300 (2019).
43. X. Liu *et al*., Bright silver brilliancy from irregular microstructures in butterfly Curetis acuta moore. *Adv. Opt. Mater.* **7**, 1900687 (2019).
44. A. Didari, M. P. Mengüç, A biomimicry design for nanoscale radiative cooling applications inspired by Morpho didius butterfly. *Sci. Rep.* **8**, 16891 (2018).
45. B. M. Boyle, T. A. French, R. M. Pearson, B. G. McCarthy, G. M. Miyake, Structural color for additive manufacturing: 3D-Printed photonic crystals from block copolymers. *ACS Nano* **11**, 3052–3058 (2017).
46. R. M. Parker *et al*., The self-assembly of cellulose nanocrystals: Hierarchical design of visual appearance. *Adv. Mater.* **30**, e1704477 (2018).
47. Z. Han, X. Feng, Z. Guo, S. Niu, L. Ren, Flourishing bioinspired antifogging materials with superwettability: Progresses and challenges. *Adv. Mater.* **30**, e1704652 (2018).
48. Z. Han, Z. Jiao, S. Niu, L. Ren, Ascendant bioinspired antireflective materials: Opportunities and challenges coexist. *Prog. Mater. Sci.* **103**, 1–68 (2019).
49. S. Tadepalli, J. M. Slocik, M. K. Gupta, R. R. Naik, S. Singamaneni, Bio-optics and bio-inspired optical materials. *Chem. Rev.* **117**, 12705–12763 (2017).
50. A. I. Miroshnikov, The longicorn beetle tribe Cerambycini Latreille, 1802 (Coleoptera: Cerambycidae: Cerambycinae) in the fauna of Asia. 2. A new or little-known species of the genus Neocerambyx J. Thomson, 1861. *Russ. Entomol. J.* **27**, 33–39 (2018).
51. S. W. Murphy, C. Oppenheimer, C. R. de Souza Filho, Calculating radiant flux from thermally mixed pixels using a spectral library. *Remote Sens. Environ.* **142**, 83–94 (2014).
52. W. Bennett, "Extreme physiology of intertidal fishes of the Wakatobi" in *Marine Research and Conservation in the Coral Triangle: The Wakatobi National Park*, J. Clifton, R. K. F. Unsworth, D. J. Smith, Eds. (Nova Science Publishers, 2010), pp. 111–128.
53. D. Lin, P. Fan, E. Hasman, M. L. Brongersma, Dielectric gradient metasurface optical elements. *Science* **345**, 298–302 (2014).
54. J. A. Schuller, T. Taubner, M. L. Brongersma, Optical antenna thermal emitters. *Nat. Photonics* **3**, 658–661 (2009).
55. A. Srinivasan, B. Czapla, J. Mayo, A. Narayanaswamy, Infrared dielectric function of polydimethylsiloxane and selective emission behavior. *Appl. Phys. Lett.* **109**, 61905 (2016).
56. Y. Fu, J. Yang, Y. S. Su, W. Du, Y. G. Ma, Daytime passive radiative cooler using porous alumina. *Sol. Energy Mater. Sol. Cells* **191**, 50–54 (2019).
57. H. Krueger, C. Killer, S. Schuett, A. Melzer, Characterization of injected aluminum oxide nanoparticle clouds in an rf discharge. *Plasma Sources Sci. Technol.* **27**, 25004 (2018).
58. R. L. Heinisch, F. X. Bronold, H. Fehske, Mie scattering by a charged dielectric particle. *Phys. Rev. Lett.* **109**, 243903 (2012).
59. W. Liu *et al*., Ultra-directional forward scattering by individual core-shell nanoparticles. *Opt. Express* **22**, 16178–16187 (2014).
60. E. M. Christenson, M. Dadsetan, A. Hiltner, A. Hiltner, Biostability and macrophage-mediated foreign body reaction of silicone-modified polyurethanes. *J. Biomed. Mater. Res. A* **74**, 141–155 (2005).